Ore Geology Reviews 105 (2019) 295–309

Contents lists available at ScienceDirect

Ore Geology Reviews

journal homepage: www.elsevier.com/locate/oregeorev

Mineralogical and geochemical features of karst bauxites from Poci (western Henan, China), implications for parental affinity and bauxitization

Shujuan Yang, Yuanxiao Huang, Qingfei Wang*, Jun Deng, Xuefei Liu, Jiaqi Wang

State Key Laboratory of Geological Processes and Mineral Resources, China University of Geosciences, Beijing 100083, China

ARTICLE INFO

Keywords:
Karst bauxite
Protolith
Mineral genesis
Bauxitization
Marine modification

ABSTRACT

The Poci bauxite deposits in western Henan, China, are hosted in the lower member of Upper Carboniferous Benxi Formation, unconformably overlying upon the paleokarst surface of the Ordovician Majiagou Formation. The orebodies comprise a high-grade bauxite horizon (characterized by the association of diaspore-illite-anatase) and a basal iron-rich horizon (diaspore-goethite-hematite-illite-anatase), sandwiched between the overlying clayey layer (illite-diaspore-goethite-anatase) and the underlying clayey layer (illite-diaspore-microcline-goethite). Geochemical investigations reveal that Rb, Cs, Ba, Cu, Zn are depleted, while B, Ga, Bi, V, Sc, Zr, Hf, Nb, Ta, W, U and Th are enriched in bauxite horizons. B is highly enriched in bauxite ores and clays (contents 176–1061 ppm) and positively associated with SiO_2, indicating B is mainly hosted in clay components, e.g. dominantly illite, which are considered a mixture of authigenic minerals transformed from kaolinites during diagenesis and unaltered detrital minerals. Mass change calculations reveal that Hf, Zr, Nb, Ta, U, Th, Sc, Cr, and Ga are stable relative to TiO_2 during the bauxitization process, indicating these elements are mainly associated with anatase and diaspore. The bauxite horizons and the underlying clays are more enriched in total REE contents (ΣREEs) and display more intense LREE/HREE fractionation than the overlying clays. Provenance analysis shows that parental materials of Poci bauxites were mainly derived from felsic-dominated igneous rocks along the southern margins of the North China Craton, with minor contribution from siliciclastic sedimentary rocks and argillaceous components of underlying carbonates. A conceptual model is proposed for the formation and evolution of Poci bauxites. Uplift caused by the North Qinling orogenesis along the southwestern margin of NCC led to the formation of karstic topography, allowing aluminum-rich source materials to be transported to the low karst plain and transformed into incipient bauxites under hot and humid tropical conditions. When the platform was submerged, Fe^{2+} ions were released from Fe/Al oxides/hydroxides under the reducing conditions associated with bacteria activity in an organic-rich environment, and redeposited as pyrites and siderites, generating a high-grade bauxite horizon and an iron-rich bauxite horizon. This marine modification resulted in further aluminum enrichment of bauxite ores.

1. Introduction

Bauxites are residual deposits that formed from intense continental subaerial weathering and alteration, generally under humid tropical to subtropical climates (Bárdossy, 1982). Three main genetic types were proposed: 1) Lateritic bauxites, predominantly gibbsitic and derived by in situ lateritization of underlying aluminosilicate rocks; 2) Tikhvin-type bauxites, overlying the eroded surface of aluminosilicate rocks, and being the erosional products of pre-existing lateritic bauxites; 3) Karst bauxites, containing boehmite and/or diaspore as the main Al minerals, developed on exhumed carbonate platforms (Bárdossy, 1982; Bárdossy and Combes, 1999; Ahmadnejad et al., 2017). Over 1 billion tons of bauxite ores have been exploited in western Henan, which are developed at the base of the Upper Carboniferous Benxi Formation. These bauxites occur on the paleokarst surface of the Cambrian to Ordovician carbonates, and are thus considered as karst type. Their formation is related to a hiatus enhanced by the long-term regional uplift and local tectonism since Middle Ordovician in the North China Craton (NCC). Although numerous studies of mineralogy, geochemistry and provenance analysis have been carried out on Henan bauxites (Wang et al., 2012; Liu et al., 2013; Wang et al., 2016 and references herein), many questions still remain controversial, e.g. the nature of precursor rocks, the elemental behaviors and the controlling factors of the bauxitization process. Provenance analysis shows that detrital zircons of the bauxite deposits in NCC were mostly derived from ~450 Ma igneous rocks of the North Qinling arc terrane along the southern

* Corresponding author.
E-mail address: wqf@cugb.edu.cn (Q. Wang).

https://doi.org/10.1016/j.oregeorev.2018.12.028
Received 17 August 2018; Received in revised form 10 December 2018; Accepted 30 December 2018
Available online 31 December 2018
0169-1368/

margin of the NCC and from the ~330 Ma intermediate-felsic plutons along its northern margin (Wang et al., 2016), indicating major contribution of aluminum-rich materials for the Henan bauxites. The regional Precambrian rocks in the paleo-uplands and the underlying Paleozoic carbonates and shales could also have provided materials for the bauxites. In this paper, we report new mineralogical and geochemical data from Poci bauxite deposits in western Henan and use these evidences to identify parental affinity, calculate mass change, reevaluate the elemental behaviors during weathering and bauxitization processes, and determine post-depositional alterations.

2. Geological setting

2.1. Regional geology

Western Henan is located in the southern North China Craton, to the north of North Qinling orogenic belt (Wang et al., 2012; Liu et al., 2013). The Archean to Paleoproterozoic crystalline basement is overlain by the Meso-Late Proterozoic meta-sedimentary strata, which in turn are covered by dominantly carbonates and clastic rocks of Cambrian to Middle Ordovician age. NCC experienced a long sedimentary hiatus of 150 Ma since the Middle Ordovician and was subjected to denudation and subaerial weathering until the deposition of the Upper Carboniferous Benxi Formation (Fig. 1). The basal Member of Benxi Formation is composed of clay and iron-aluminum-rich sediments, overlain by clastic-carbonate sequences of the upper Bangou Member of Benxi Formation. These formations are followed by coal-bearing clastic-carbonate deposits of the Upper Carboniferous Taiyuan Formation and by thick Permian-Triassic terrestrial clastic deposits (Liu et al., 2013; Wang et al., 2016). The basement and the above strata were widely deformed, and exposed mainly in the southwest mountain areas and central hills of Henan Province. The regional geology has been elaborated by Liu et al. (2013) and Wang et al. (2016).

2.2. Geology of the Poci bauxite deposits

The Poci bauxite deposits occur in karst depressions or dolines, vary in thickness from several meters to tens of meters, and are usually controlled by the paleokarst topography (Figs. 2 and 3). The high-grade bauxite horizon passes into an iron-rich bauxite horizon and then to a clayey layer both downward and laterally of the deposits. These horizons are overlain by a clayey layer and then by stratiform carbonates: a situation that is identical to the Guangou and Jiagou bauxites (Liu et al., 2013; Wang et al., 2016). The bauxite ores are dominated by clastic, pisolitic-oolitic, nodular, and spongy textures in a pelitomorphic and cryptocrystalline matrix (Fig. 4).

3. Sampling and analysis methods

Six bauxite ore samples, 6 clay samples from both underlying and overlying clayey layers, as well as carbonate samples from the rock units below and above the deposits, were collected from two profiles (Figs. 2 and 3).

Mineralogical and textural studies were carried out using optical microscopy and X-ray diffraction (XRD) at China University of Geosciences (Beijing) and in the Laboratory of Petroleum Geology Research Center (Beijing), respectively. XRD analyses were conducted on a graphite monochromator using a Japanese Rigaku D/Mac-RC model with Cu Kα1 radiation at voltage of 40 kV, a beam current of 80 mA, scanning speed of 8°/min, slit DS = SS = 1°. The semi-quantitative mineralogical analysis of analyzed samples (in mass %) were measured using an internal corundum reference, according to the basic principles and procedure of quantitative analysis described in detail by Snyder and Bish (1989).

SEM-EDX microanalysis was also carried out to analyze the mineral phases at China University of Geosciences (Beijing), on a Hitachi S-3400 N scanning electron microscope equipped with a Link Analytical Oxford IE 350 ED X-ray spectrometer.

All samples were pulverized to 200-mesh using an agate mill for

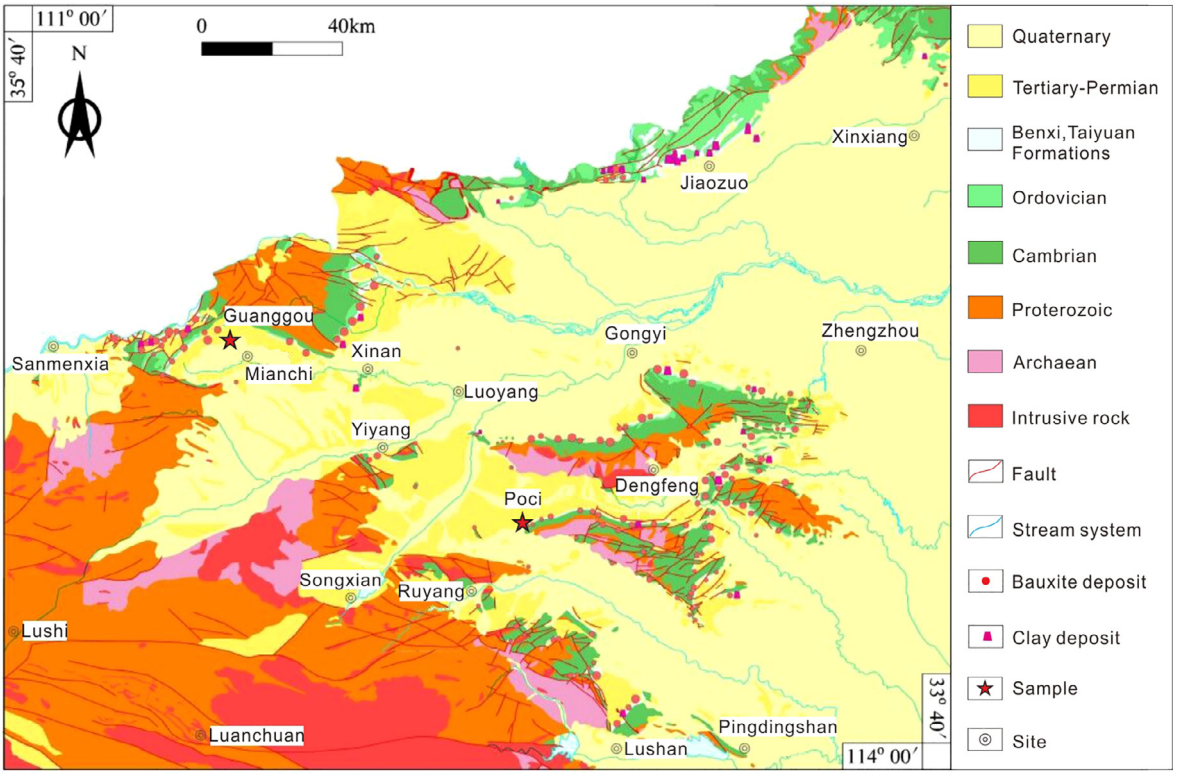

Fig. 1. Geological map of Poci bauxites in western Henan.

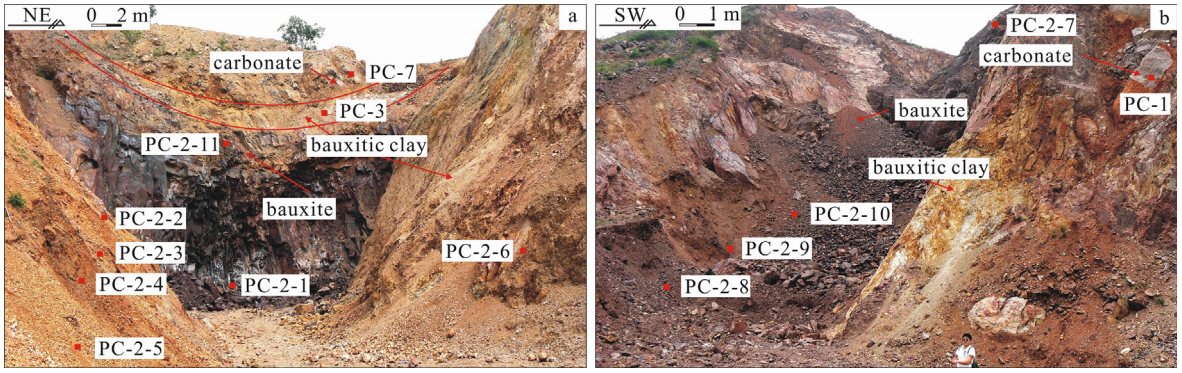

Fig. 2. Field photographs of two Poci bauxite profiles occuring in a paleokarst sinkhole (a) and a paleokarst valley (b) showing samplings.

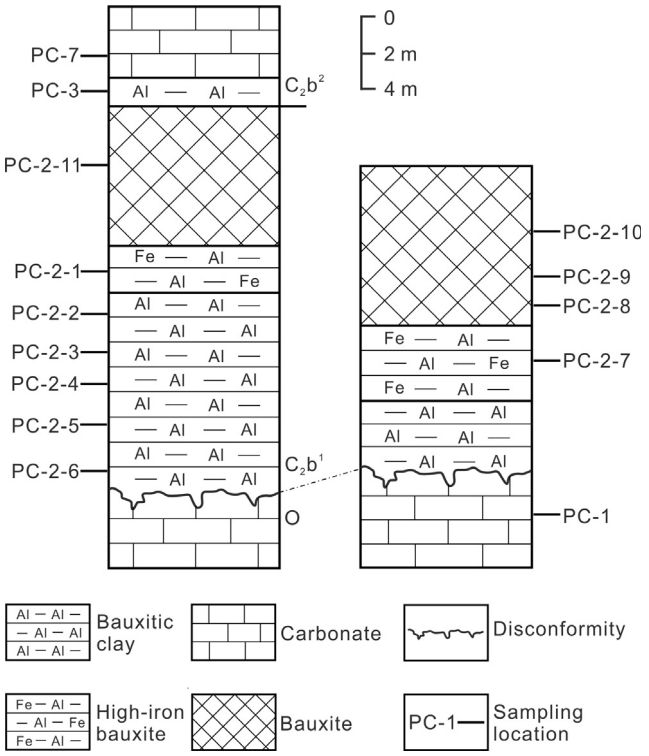

Fig. 3. Stratigraphic column of the Poci bauxite profiles.

whole-rock chemical analysis at the Analytical Laboratory of the Geological Survey of China in Langfang, Hebei Province. Major elements in whole rocks (except FeO and total loss ignition) were determined by standard X-ray fluorescence (XRF) on a spectrometer with Philips Model 1480 and a Rh tube. The FeO contents were analyzed by using the volumetric method; the total loss in ignition was determined by weight difference and the potentiometry method. Trace element contents (S, B, F, Li, Rb, Cs, Be, Sr, Ba, Cu, Zn, Ga, Bi, Ni, Cr, V, Sc, Zr, Hf, Nb, Ta, W, Th, and U) were analyzed on inductively coupled plasma-mass spectrometry (ICP-MS), emission spectrography (ES), and XRF. Detection limits for major elements were ≤0.1 wt%, for most trace elements ≤2 ppm, for Cr, Rb, Sr, and V ~5 ppm, for F and S 100 and 50 ppm, and for REEs < 0.3 ppm.

4. Results

4.1. Mineralogy

The XRD and semi-quantitative mineralogical analysis revealed that the bauxite ores are mainly composed of diaspore (42–74.5 wt%) and illite (15.8–52.9 wt%), with subordinate anatase, occasionally traces of hematite, goethite, kaolinite, and zircon (Table 1, Fig. 5). Large quantities of hematite (18.2–34.2 wt%) and small amounts of goethite (4.9 wt%) are restricted to the basal iron-rich bauxite horizon. Back-scattered electron images of bauxite ores show that diaspore and illite occur widely in the matrix, pisolites and concentric ooids (Fig. 6). Both underlying and overlying clays comprise mainly illite (69.3–100 wt%), which interleaves with small quantities of diaspore and minor iron minerals. Microcline was only detected in the deepest clay sample of the underlying clayey layer, with a weight percentage of 30%.

4.2. Geochemistry

The chemical compositions of the analyzed samples are shown in Table 2. The bauxite ores are mainly composed of Al_2O_3 (51.11–71.04 wt%), SiO_2 (6.30–23.22 wt%), and TiO_2 (2.33–3.46 wt%), with variable Fe_2O_3 contents (0.42–1.55 wt% in the high-grade bauxite horizon and 25.55–33.74 wt% in the iron-rich bauxite horizon), small amounts of K_2O (1.85–5.81 wt%) and P_2O_5 (0.08–0.18 wt%) and negligible amounts of MgO, CaO, Na_2O and MnO. By contrast, the clay samples contain much higher SiO_2 (38.91–51.43 wt%) and K_2O (9.44–11.13 wt%), lower Al_2O_3 (30.03–39.84 wt%). Binary diagrams of major oxides show a strongly positive correlation between Al_2O_3 and TiO_2 (with a correlation coefficient of $R^2 = 0.89$), and the correlation lines pass through the underlying and overlying carbonates, whereas negative correlations are found between Al_2O_3 and SiO_2 ($R^2 = 0.78$) (Fig. 7).

Correlation analysis reveals that high field strength elements (Hf, Zr, Nb and Ta) are positively associated with TiO_2 contents (Fig. 8). The upper continental crust (UCC) and post-Archean Australian shale (PAAS)-normalized patterns of trace elements (Fig. 9a) reveal that the bauxite and clay samples are slightly different and both are more enriched in trace elements than carbonates, except for Sr, Cu, and Zn (Fig. 9b). Boron is highly enriched in bauxite ores and clay samples with contents ranging from 176 to 1061 ppm.

The carbonates and the overlying clay are characterized by low ΣREE contents (13–57 ppm), while the bauxite horizons and underlying clays contain much higher ΣREE contents (185–755 ppm) (Table 2). The UCC-normalized REE patterns are flat and identical to the PAAS-normalized results, both showing that the overlying clayey layer is depleted in LREEs relative to the bauxite horizons and the underlying clayey layer (Fig. 10a and b). The chondrite-normalized REE patterns also reveal that LREEs are more fractionated within the three layers of the bauxite profiles than HREEs (Fig. 10c): all samples are highly enriched in LREEs relative to HREEs with $(La/Yb)_N$ ratios ranging from 3.65 to 18.10, except the overlying clay sample with an extremely low $(La/Yb)_N$ ratio of 1.83 (Table 2). All samples are characterized by negative Eu anomaly, with Eu/Eu* ranging from 0.64 to 0.71 in carbonates and the overlying clays, 0.54–0.63 in the underlying clays and 0.49–0.58 in bauxites ores (Table 2). The iron-rich bauxite horizon has

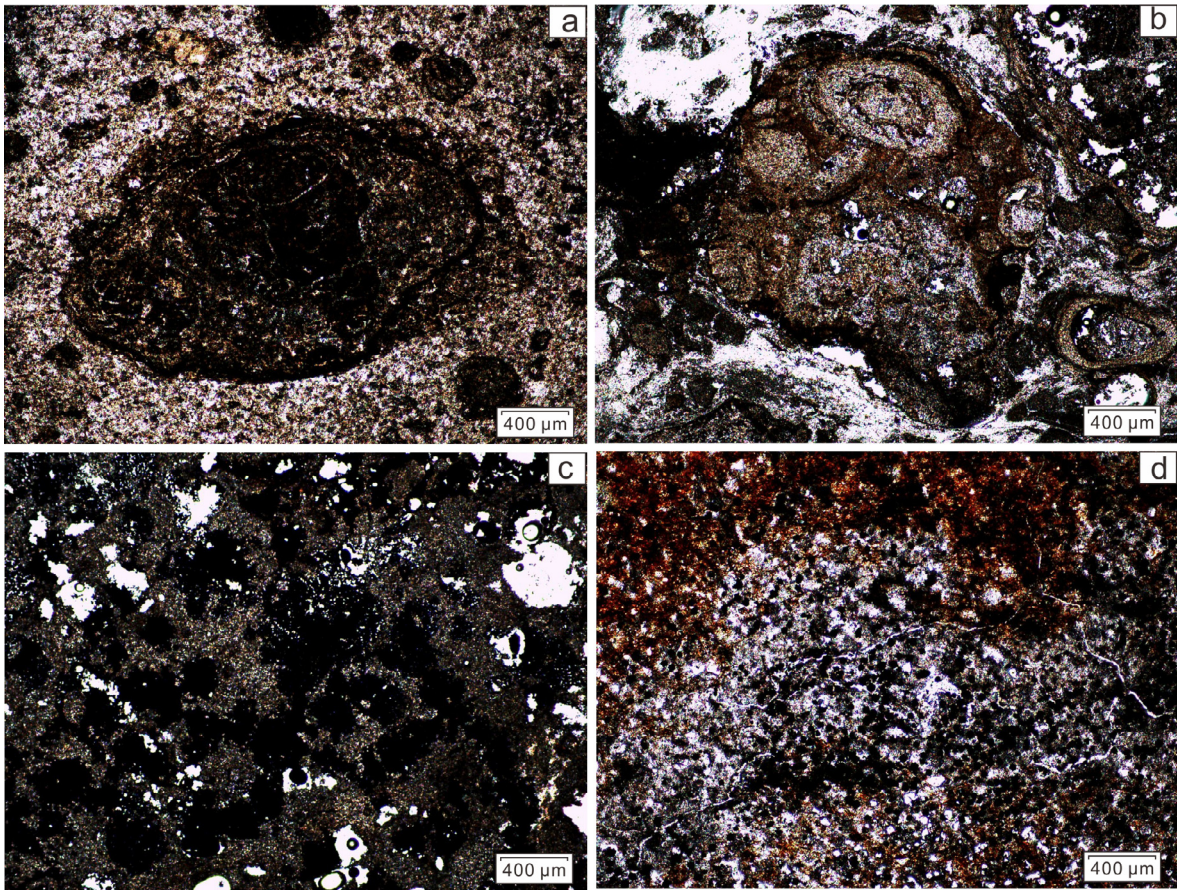

Fig. 4. Photomicrographs of the bauxite ores and clay sample: (a) pisolite in the pelitomorphic and cryptocrystalline matrix; (b) clastic texture showing nodules with complex internal ooids; (c) and (d) iron-minerals in the illitic matrix.

Table 1
Semiquantitative mineralogical analysis of bauxite and clay samples (in mass wt%).

Sample	Lithology	K-feldspar	Calcite	Anatase	Diaspore	Hematite	Goethite	Illite	Kaolinite
PC-3	Clay	–		–	6.30	–	–	93.70	–
PC-2-2	Clay	–	–	–	9.90	–	–	90.10	–
PC-2-3	Clay	–	–	–	3.00	–	–	97.00	–
PC-2-4	Clay	–	–	–	2.00	–	–	98.00	–
PC-2-5	Clay	–	–	–	–	–	–	100.00	–
PC-2-6	Clay	30.70	–	–	–	–	–	69.30	–
PC-2-1	Iron-rich Bauxite	–	–	–	57.40	18.20	4.90	17.20	2.30
PC-2-7	Iron-rich Bauxite	–	–	4.00	46.00	34.20	–	15.80	–
PC-2-8	Bauxite	–	–	5.30	62.30	–	–	32.40	–
PC-2-9	Bauxite	–	–	5.10	42.00	–	–	52.90	–
PC-2-10	Bauxite	–	–	5.30	54.80	–	–	37.50	2.40
PC-2-11	Bauxite	–	1.80	1.20	74.50	–	–	22.50	–

strongly positive Ce anomalies (Ce/Ce* = 2.56–3.85), relative to slightly positive values in the high-grade bauxite horizon (Ce/Ce* = 1.11–1.80) (Table 2). Correlation analysis displays a strongly positive correlation between Ce contents and La/Y ratios (Fig. 11a), ΣREEs and P_2O_5 contents (Fig. 11b), respectively.

Mass change calculations have been carried out for the bauxites and underlying clays, with respect to potential parent rocks (i.e. felsic volcanics and PAAS) in order to constrain the geochemical processes involved in the development of Poci bauxites. The mass changes were calculated with Ti as the immobile element by using the equations presented by Calagari and Abedini (2007). Both bauxite horizons and the underlying clays show a depletion in nearly all major, minor and trace elements relative to Ti, except Cr and V, which show a slight enrichment, when compared with felsic volcanics (Condie, 1993) (Fig. 12), while REEs show strong fractionation between the bauxites and underlying clays when compared to PAAS (Fig. 13).

Clustering analysis was also adopted to evaluate the element associations and behaviors. Seven major clusters with correlation coefficients greater than 0.7 are revealed: (1) REEs-P_2O_5, (2) B-Rb-F-Ba-SiO_2, (3) Li-Cs, (4) S-Cu-Be-Zn-Ni, (5) Zr-Hf-U-Cr-Ga-Th-Nb-Ta-TiO_2-Al_2O_3, (6) Bi-V, and (7) Fe_2O_3-Ce/Ce*-Sc (Fig. 14).

5. Discussion

5.1. Parental affinity

Sm/Nd ratios and Eu anomalies have been applied to identify the provenance of bauxites, for these elements show minor fractionation

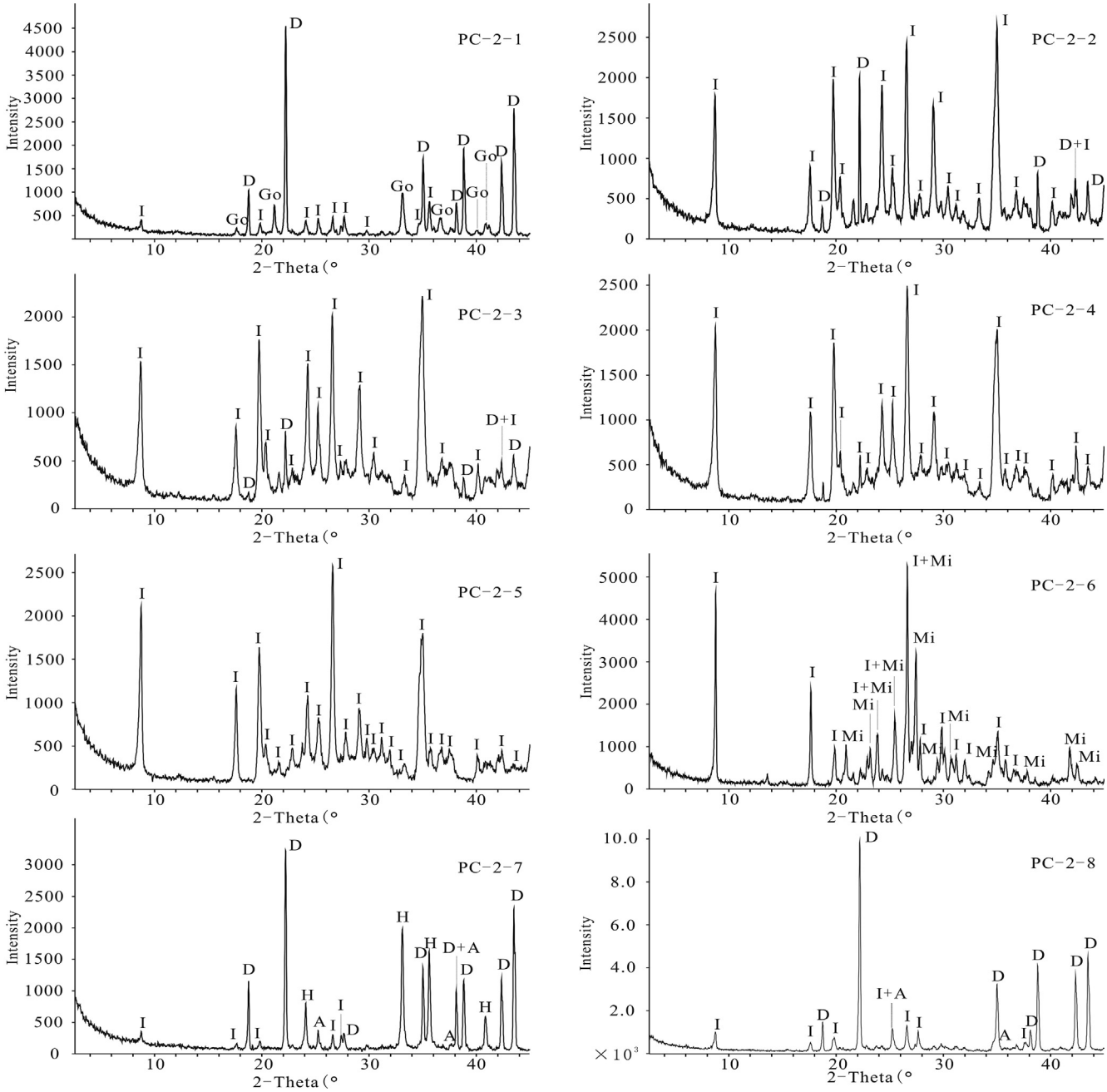

Fig. 5. XRD patterns of the analyzed samples. (A-anatase, D-diaspore, Go-goethite, H-Hematite, I-illite, Mi-microcline).

during the intense chemical weathering (Mongelli et al., 2006; Mameli et al., 2007; Ahmadnejad et al., 2017). Guangou bauxite deposit is located 110 Km northwest of the Poci area and has been developed in geological settings similar to that of Poci bauxite profiles. For this reason, the REE data were cited from Liu et al. (2013) and used for Sm/Nd-Eu/Eu* plotting, to make sedimentary correlation and provenance analysis.

The carbonate bedrocks of the Guangou deposit display variable Sm/Nd ratios and distinctive features in the Sm/Nd-Eu/Eu* binary diagram, denying their parental affinities with the bauxites (Fig. 15). However, a minor contribution from argillaceous components of the underlying limestones is still possible. Both the Guangou and Poci bauxites and clays plot close to felsic volcanic rocks, PAAS, cratonic sandstones and greywackes, indicating that the parental materials were mainly derived from felsic-dominated igneous rocks and siliciclastic sedimentary rocks. This inference is also supported by the diagram of Cr against Ni (Fig. 16) and consistent with the multiple U-Pb age peaks of the Late Carboniferous karst bauxites from NCC in Wang et al. (2016). These evidences confirm multiple origins: the detrital zircons with ages at ~450 Ma were mostly derived from igneous rocks of the North Qinling arc terrane along the southern margin of the NCC, those with ~330 Ma ages from intermediate-felsic plutons along the northern margin, while the older detrital zircon components might be likely inherited from reworked old crustal materials.

Mass change calculations relative to TiO_2 values revealed similar element behaviors between the bauxites and underlying clays with respect to felsic volcanics. However, a different pattern was found for the results with reference to PAAS values: LREEs show strong fraction between the bauxites and the underlying clays, with La and Nd being lost in the bauxite horizons but highly enriched in the underlying clays. Although some researchers suggest that REEs are variably mobile and fractionate during pedogenesis (Braun et al., 1990, 1993; Laveuf and

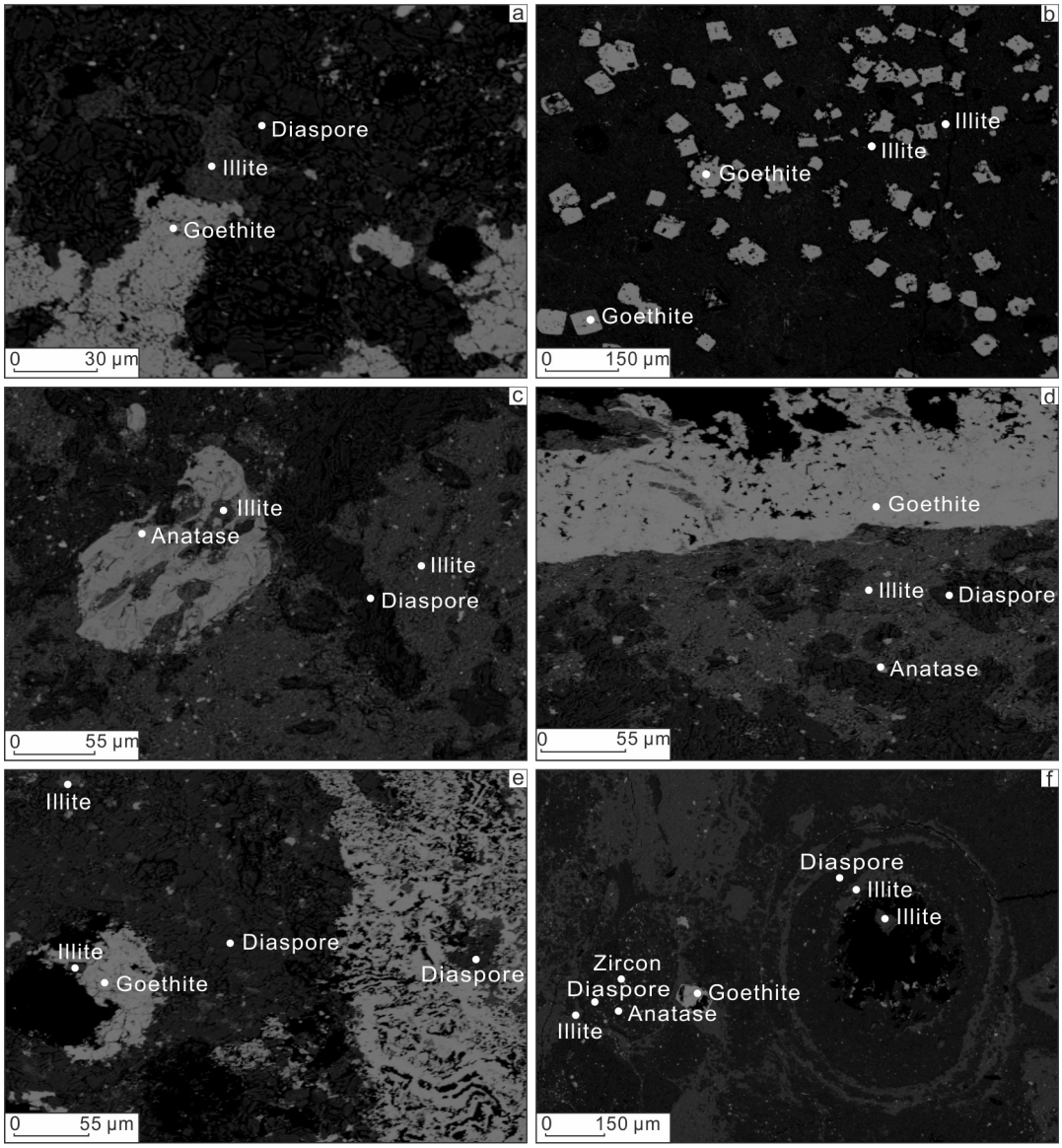

Fig. 6. Backscattered electron images of the underlying clays (a and b), the overlying clays (c and d) and bauxite ores (e and f): (a) goethite coexisting with diaspore and illite; (b) cubic goethite pseudomorphs after pyrite in the illitic matrix; (c) diaspore coexisting with illite and anatase; (d) goethite veins penetrating bauxite ores; (e) diaspore coexisting with goethite and illite; (f) alternating diaspore and illite layers in an ooid.

Cornu, 2009; Babechuk et al., 2014), the reverse behavior of REEs between the bauxites and the underlying clays is unreasonable. This implies that the parent materials of Poci bauxites are more of felsic nature than clastic sedimentary rocks.

Karst bauxite deposits are widely distributed in North China, and uniformly formed during the Late Mississippian–Middle Pennsylvanian, reflecting prolonged uplift and exposure of the North China Craton. During the Middle Ordovician-Late Carboniferous hiatus, the NCC experienced extensive geographic and geological changes: it was separated from the northern margin of Gondwana during the Devonian, drifted across the equator and northward to the tropics of the eastern Paleo-Tethys ocean with paleolatitudes of ca. 5–9°N by the Late Carboniferous (Yu et al., 2018), and then was accreted with North Qinling and Bainaimiao arc systems along the west-southern and northern margins by the Late Paleozoic (Wang et al., 2016). The accretion caused the topographic uplift along the convergent margins, which led to the formation of karstic topography, allowing aluminum-rich source materials to be transported to the low karst plain, weathered and accumulated as Al/Fe oxides/hydroxides-rich incipient bauxite materials along the coast under hot and humid tropical conditions. The formation of the Late Carboniferous bauxite deposits within the NCC is the result of the integrated tectonic, paleogeographic, and paleoclimatic changes exerting on the large karst basin.

5.2. Elemental behaviors and controlling factors

For determination of the elemental behaviors and potential host minerals for trace elements and REEs in the Poci bauxites, mass change calculations and clustering analysis based on correlation coefficients have been carried out for major, minor, trace and rare earth elements. Certain element groups can be used to track the pathways of transportation, migration, transformation and fixation during the intense weathering processes.

5.2.1. Trace elements

Alkali and alkaline earth elements are the most often released to solution during chemical weathering, and are usually or almost exclusively adsorbed on clay minerals such as smectite and illite, yielding

Table 2
Geochemical composition of the analyzed samples.

Sample	Overlying carbonate	Overlying clays	High-grade bauxite horizon				Fe-rich bauxite horizon		Underlying clays					Underlying carbonate
	Pc-7	Pc-3	Pc-2-11	Pc-2-10	Pc-2-9	Pc-2-8	Pc-2-7	Pc-2-1	Pc-2-2	Pc-2-3	Pc-2-4	Pc-2-5	Pc-2-6	Pc-1
SiO_2 (%)	0.13	38.91	7.61	15.69	23.22	13.48	6.3	8.72	41.65	41.96	43.2	43.18	51.43	0.78
Al_2O_3	0.24	39.84	71.04	63.59	61.98	68.37	51.11	56.2	39.27	38.14	38.12	35.19	30.03	0.79
Fe_2O_3	0.22	2.4	0.49	1.55	0.91	0.42	33.74	25.55	0.27	0.51	0.36	3.37	1.77	0.97
FeO	0.11	0.24	0.15	0.19	0.08	0.22	0.21	0.16	0.17	0.11	0.08	0.15	0.15	0.17
MgO	0.4	0	0	0	0	0	0	0	0	0	0	0.06	0.16	21.9
CaO	55.62	0.1	1.03	0.01	0.02	0.01	0.04	0.02	0.06	0.1	0.1	0.1	0.07	33.39
Na_2O	0.01	0.02	0.01	0.08	0.11	0.01	0.05	0.03	0.02	0.04	0.02	0.04	0.04	0.01
K_2O	0.05	9.44	1.93	3.65	5.81	3.31	1.37	1.85	10.38	10.3	10.54	10.56	11.13	0.19
MnO	0.17	0	0.01	0.03	0.01	0.03	0.01	0.12	0	0	0	0.03	0.04	0.03
P_2O_5	0.04	0.06	0.08	0.18	0.09	0.19	0.1	0.09	0.09	0.1	0.15	0.12	0.24	0.01
TiO_2	0.02	2.79	3.46	2.98	2.91	2.93	2.69	2.33	1.6	2.03	1.82	1.28	0.79	0.08
H_2O+	0.79	6.21	13.09	11.51	4.09	10.97	3.85	3.83	5.55	5.83	5.57	5.36	2.93	0.06
CO_2	41.6	0.33	1.36	0.31	0.31	0.19	0.38	0.45	0.31	0.22	0.19	0.22	0.3	42.31
L0I	42.39	6.55	14.45	11.82	4.39	11.16	4.23	4.29	5.86	6.05	5.76	5.57	3.23	42.37
S (ppm)	477	246	263	745	258	523	479	206	191	154	165	145	2416	109
B	1	613	353	476	431	316	265	176	743	704	1061	916	622	16
F	84	776	520	541	563	480	688	443	840	875	746	840	1026	118
Li	1.9	28.5	4.9	14.8	19.9	17.7	7.7	20.8	68.7	65	31	32.8	11.1	5
Rb	2	216	36	87	130	64	23	32	262	224	292	277	228	6
Cs	0.4	6.6	0.5	2.3	3.6	2.0	0.6	0.8	10.7	11.9	12.1	7.9	0.8	0.4
Be	1	2	1	2	3	3	1	1	5	5	5	5	23	1
Sr	402	64	293	798	390	850	435	344	346	355	784	580	357	84
Ba	10	51.6	19.7	80.1	63.6	74.2	12	68	76	95.5	95.5	94.5	146.1	33.4
Cu	10	47	35	58	7	14	27	22	8	22	5	5	137	7
Zn	12	24	13	30	28	21	37	42	10	26	10	33	111	12
Ga	6.3	61.4	60.5	67.1	48.1	60.6	66.5	65.1	29.4	20.9	30.8	33.1	23.2	5.4
Bi	0.1	1.9	1.0	3.3	0.7	0.7	0.8	1.0	0.9	1.0	0.5	0.4	1.0	0.1
Ni	10	7	14	69	34	41	15	40	10	34	17	59	143	5
Cr	18	150	200	296	182	229	181	148	133	152	116	123	94	19
V	11	151	142	862	337	421	391	223	152	282	328	203	64	24
Sc	1.5	17.3	35.2	42.9	24.4	24.3	84.9	43.3	20.5	27.3	20.3	24.4	17.1	2.9
Zr	6.0	697.2	910.2	702.3	699.3	571.4	473	434.7	456.7	495.9	419.7	361.2	136.4	11.9
Hf	0.2	19.0	22.7	18.0	17.7	14.2	11.9	12.5	13.0	13.0	11.1	10.9	3.8	0.4
Nb	1.6	63.7	32.3	55.2	55.1	59	35.7	32.6	47.8	55.5	55.5	35.2	18.6	1.5
Ta	0.1	5.1	2.5	4.3	4.1	4.5	2.8	2.8	3.6	4.3	4.0	2.7	1.5	0.1
W	0.2	3.2	4.5	8.1	16.8	12.0	2.6	2.7	6.4	3.8	35.0	30.5	14.2	0.3
Th	4.8	55.2	83.4	93.8	67.9	82.6	20.9	41.2	44	46.2	63.6	45	38.5	6.3
U	2.14	13.95	16.61	15.94	13.26	15.74	14.58	12.2	13.04	17.24	9.17	4.67	3.95	0.71
La	2.95	8.58	39.02	146.18	58.68	154	31.5	16.6	66.02	104.35	125.53	100.88	113.91	7.43
Ce	5.45	24.58	117.73	496.22	144.26	367.83	161.29	131.72	154.33	233.03	282.19	254.17	220.51	8.12
Pr	0.54	1.86	9.02	26.17	14.06	39.54	6.68	3.8	17.08	29.8	29.79	24.92	28.33	0.98
Nd	1.88	6.08	33.46	74.11	54.55	135.87	22.68	13.93	57.39	113.4	104.2	92.02	102.59	2.93
Sm	0.39	1.45	5.61	7.98	10.51	16.76	4.04	3.08	9.91	20.43	16.88	19.19	16.74	0.61
Eu	0.09	0.37	0.89	1.32	1.78	2.31	0.69	0.61	1.78	3.75	2.84	3.58	2.68	0.13
Gd	0.38	1.74	4.04	8.34	7.74	10.13	3.83	3.31	6.91	15.27	11.89	14.55	12.75	0.62
Tb	0.07	0.51	0.89	1.49	1.4	1.69	0.67	0.66	1.08	2.6	1.6	2.24	2.48	0.12
Dy	0.39	3.73	5.71	9.33	7.73	8.98	4.07	4.12	5.06	13.08	6.81	10.36	14.68	0.72
Ho	0.08	0.83	1.29	2.09	1.61	1.87	0.87	0.88	0.87	2.23	1.26	1.84	2.99	0.15
Er	0.23	2.56	4.04	6.64	4.96	6.11	2.69	2.67	2.43	5.63	3.85	4.97	8.41	0.41
Tm	0.03	0.46	0.72	1.21	0.89	1.09	0.48	0.46	0.39	0.86	0.66	0.77	1.24	0.07
Yb	0.2	3.24	5.07	8.57	6.11	7.75	3.31	3.15	2.7	5.75	4.8	5.02	7.22	0.43
Lu	0.03	0.52	0.81	1.35	0.97	1.27	0.53	0.5	0.43	0.87	0.78	0.78	1.05	0.08
Y	3.99	22.21	33.65	47.11	37.53	44.52	24.06	24.98	19.76	42.74	29.77	43.53	93.87	4.73
ΣREE	12.7	56.51	228.3	791	315.25	755.2	243.34	185.49	326.39	551.05	593.08	535.29	535.58	22.79
ΣLREE	11.29	42.92	205.73	751.98	283.84	716.31	226.88	169.74	306.52	504.76	561.43	494.77	484.76	20.2
ΣHREE	1.41	13.59	22.57	39.02	31.41	38.88	16.46	15.75	19.87	46.28	31.65	40.53	50.82	2.59
$\Sigma LREE_{(La-Eu)}/\Sigma HREE_{(Gd-Lu)}$	8.02	3.16	9.11	19.27	9.04	18.42	13.79	10.78	15.43	10.91	17.74	12.21	9.54	7.79
Ce/Ce*	0.97	1.42	1.46	1.8	1.17	1.11	2.56	3.85	1.08	0.99	1.08	1.19	0.91	0.63
Eu/Eu*	0.7	0.71	0.54	0.49	0.57	0.5	0.52	0.58	0.62	0.62	0.58	0.63	0.54	0.64
$(La/Yb)_N$	10.21	1.83	5.33	11.81	6.65	13.76	6.59	3.65	16.93	12.56	18.11	13.91	10.92	11.97
$(La/Sm)_N$	4.76	3.71	4.36	11.48	3.5	5.76	4.88	3.38	4.17	3.2	4.66	3.29	4.27	7.65
$(Gd/Lu)_N$	1.64	0.41	0.62	0.76	0.98	0.99	0.89	0.83	1.99	2.18	1.88	2.3	1.5	1.01
La/Y	0.74	0.39	1.16	3.1	1.56	3.46	1.31	0.66	3.34	2.44	4.22	2.32	1.21	1.57

significant compositional variations relative to the unaltered parent rocks. Mass change calculations reveal that Rb, Sr and Ba are depleted elements in the bauxites and underlying clays relative to TiO_2 when derived from felsic volcanics (as the accepted precursor). Both bauxites and clays have elevated boron contents (176–1061 ppm), much higher than average contents in soils (9–88 ppm, Kabata-Pendias and Pendias, 2001). Boron values are highly positively correlated with SiO_2 ($R^2 = 0.81$), suggesting that boron is mainly hosted in the clay components (e.g. dominantly illite in this study). Illite is an initial primary host for large ion lithophile elements such as cesium, barium, rubidium (Williams et al., 2001), which can readily substitute potassium in illite. Boron is significantly enriched in the bauxites of western Henan (Wang

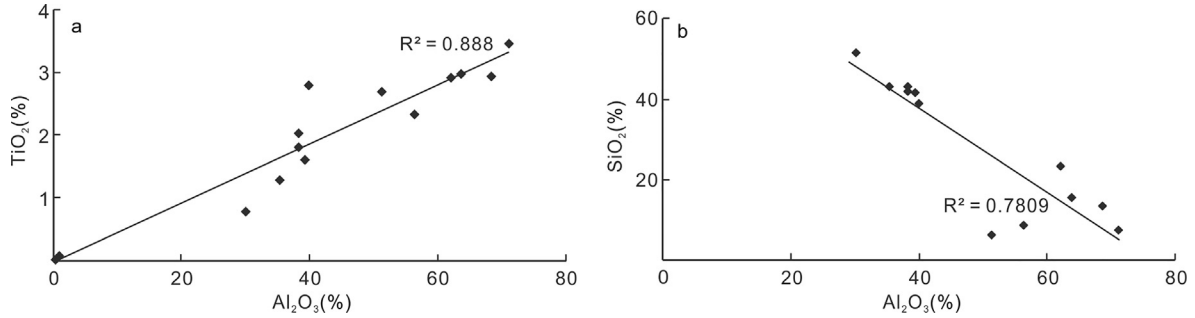

Fig. 7. Correlation analysis between TiO_2 and Al_2O_3 (a) and SiO_2 and Al_2O_3 (b).

et al., 2012; Liu et al., 2013), compared to other karst bauxite deposits of the world. It is known that all the major clay minerals may contain boron, and illite usually contains the most boron and kaolinite the least (Harder, 1970; Couch, 1971). Boron is a highly mobile element, preferring aqueous phases to that of most minerals, and can be adsorbed onto the surfaces or incorporated into tetrahedral sites of authigenic illite to substitute for silicon (Williams et al., 2001). Although some of the variation in the boron contents of sediments from apparently homogeneous depositional environments may be due to different boron contents in weathered materials (Lerman, 1966), the extremely high contents of boron can serve as a critical geochemical indicator of marine environment (Harder, 1970). Besides, adsorption of boron on clay minerals is a function of boron content in solution and pH, and the maximum occurs only under alkaline conditions at approximately pH 9.0–9.7 (Keren and Mezuman, 1981; Goldberg et al., 1993), suggesting that the acidic condition of meteoric water flow is not favorable for the adsorption of boron on clay minerals while a marine depositional environment is to the benefit of boron adsorption. Therefore, the high abundance of boron in the bauxites of western Henan could result from extraction by illite minerals from seawater in addition to inheritance from the underlying boron-rich potential protoliths as proposed by Wang et al. (2012).

The high field strength elements (HFSEs: Hf, Zr, Nb and Ta), as well as U, Th, Sc, Cr, and Ga are enriched relative to the UCC and PAAS (Fig. 9). Mass change calculations from both felsic volcanics and PAAS reveal these elements are very stable relative to TiO_2 components (Figs. 12 and 13). These geochemical signatures suggest that Hf, Zr, Nb,

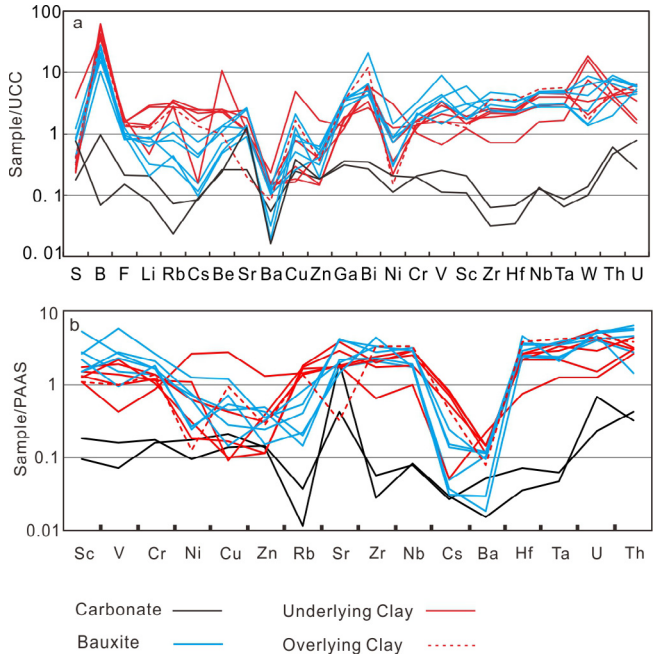

Fig. 9. Upper continental crust and PAAS-normalized trace element spidergrams.

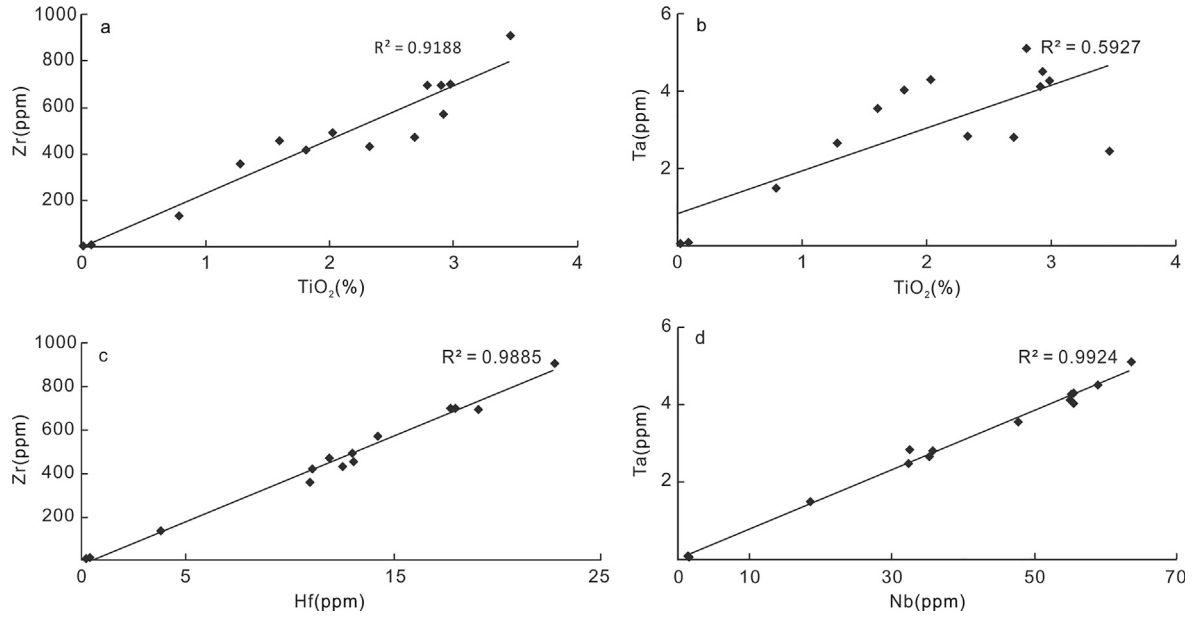

Fig. 8. Correlation analysis between Zr and TiO_2 (a), Ta and TiO_2 (b), Zr and Hf (c), and Ta and Nb (d).

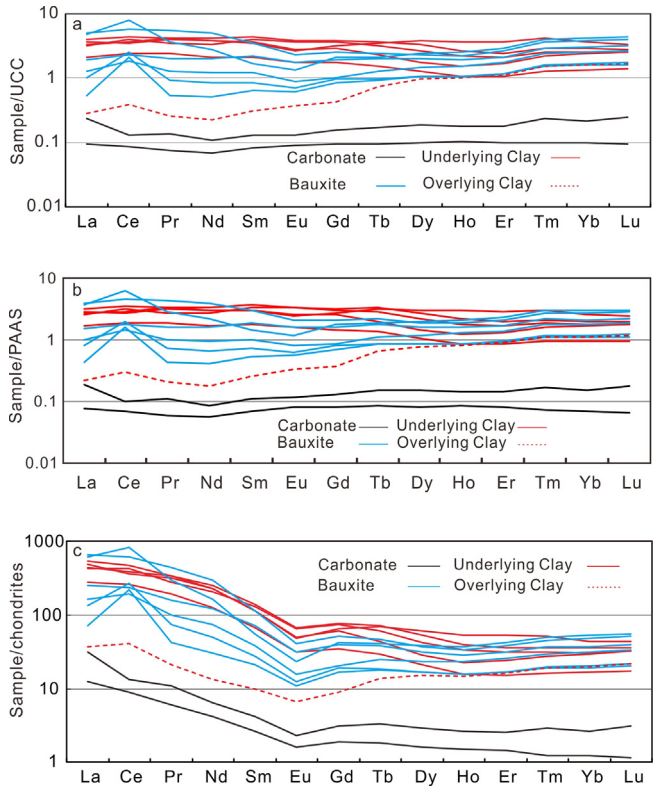

Fig. 10. UCC (a), PAAS (b) and chondrite (c)-normalized REE patterns.

Ta, U, Th, Sc, Cr, and Ga have similar geochemical behavior and are relatively immobile during the bauxitization process and the HFSEs are mainly hosted in anatase and diaspore, and, to a lesser extent, in unaltered detrital minerals such as zircon and rutile (Mordberg et al., 2001; Zarasvandi et al., 2012; Liu et al., 2013).

Previous studies (Bárdossy and Aleva, 1990; Ahmadnejad et al., 2017) indicate that Ga is usually concentrated in karst bauxites and considered to be mainly hosted in boehmite and diaspore, which is also supported by the clustering analysis in this study. Cr has its maximum contents in the bauxite horizons (148–296 ppm), followed by the overlying clays and underlying clays (94–152 ppm), much higher than those of the carbonates (18–19 ppm) (Table 2), indicating geochemical concentration instead of anthropogenic contamination. Cr is often found highly enriched in bauxites, and considered as one of the "bauxitophile" elements (Mongelli et al., 2017; Putzolu et al., 2018). Although elevated Cr values are usually indicative of mafic or ultramafic origin, the provenance analysis precludes a significant contribution of materials from mafic or ultramafic rocks. The clustering of Cr and Al_2O_3 with coefficient of correlation greater than 0.9 indicates that enrichment of Cr is associated with secondary oxides and clays during weathering thanks to the similar behavior of Cr^{3+} to that of Al^{3+} and Fe^{3+} (Gamaletsos et al., 2017).

The transition metal elements are generally associated with Fe and Mn oxides, which can be usually found in soil as local concentrations of nodules. However, the accumulation of Fe and Mn oxides is not necessarily simultaneous in the chemical weathering processes. Elements fixed on active sites of oxyhydroxide surfaces are exchangeable and liable to removal by changing solution contents and pH conditions (Bauer and Velde, 2014), and the element contents are usually related to iron-manganese oxide fractionations. Consequently, the affinity of transition metal elements with Fe and Mn compounds was not found in the clustering analysis. Whereas, a close relationship with sulfur element was revealed by the element assemblage of S-Cu-Be-Zn-Ni, although those occur in sulfides tend to be readily released and transformed.

5.2.2. Rees

Although REEs display very similar chemical properties, the chondrite-normalized REE patterns reveal variable inter-elemental fractionation during different stages of weathering, pedogenesis and bauxitization (Braun et al., 1990; Laveuf and Cornu, 2009; Sanematsu et al., 2013; Babechuk et al., 2014; Ahmadnejad et al., 2017). Weathered materials are relatively enriched in LREEs over HREEs, compared to the parent rocks (Nesbitt, 1979; Ma et al., 2002). The mass change calculations from felsic volcanics show LREEs are more depleted than HREEs relative to TiO_2, also indicating LREEs are more susceptible to fractionation than HREEs. The secondary minerals such as Fe and Mn-oxides and hydroxides, phosphate minerals, clay minerals, along with some heavy detrital minerals (e.g. zircon and anatase) serve as the most important scavengers for REEs and play a critical role in concentrating of the REEs (Aubert et al., 2001; Yusoff et al., 2013; Hanilçi, 2013; Ahmadnejad et al., 2017). The overlying clayey layer contains much lower ΣREE contents than bauxite horizons and the underlying clayey layer, and shows a distinct chondrite-normalized pattern (Table 2, Fig. 10c), indicating a different protolith for the overlying clay or intensive fractionation during the downward leaching of REEs.

The chondrite-normalized REE patterns reveal that cerium behaves variously between bauxite horizons and clayey layers, and differently from other LREEs. The bauxites ores and the overlying clay sample display positive Ce anomalies, while carbonates and the underlying clays present no to negative values. Ce anomalies are highly positively related with Fe_2O_3 contents ($R^2 = 0.71$), and the clustering analysis displays an assemblage of Sc-Ce/Ce*-Fe_2O_3 (Fig. 14), indicating Ce concentrates mainly coupled with Fe-oxides notably due to high Eh (Ma et al., 2002; Laveuf and Cornu, 2009). Previous studies demonstrated that positive Ce-anomalies, over the other REEs in lateritic profiles, are mineralogically related to the precipitation of cerianite (CeO_2) in Fe and Mn-oxides under oxidative conditions (Braun et al., 1990; Mongelli, 1997; Laveuf and Cornu, 2009). The contents of cerium are also strongly and positively correlated with La/Y ratios (Fig. 11a), which generally increase with depth and have been used to determine change in pH during weathering (Maksimovic and Panto, 1991; Zarasvandi et al., 2012; Ellahi et al., 2016), suggesting that precipitation of cerium is also controlled by pH. Scandium is usually hosted in hematite, where Sc^{3+} probably substitutes Fe^{3+}, which interprets its

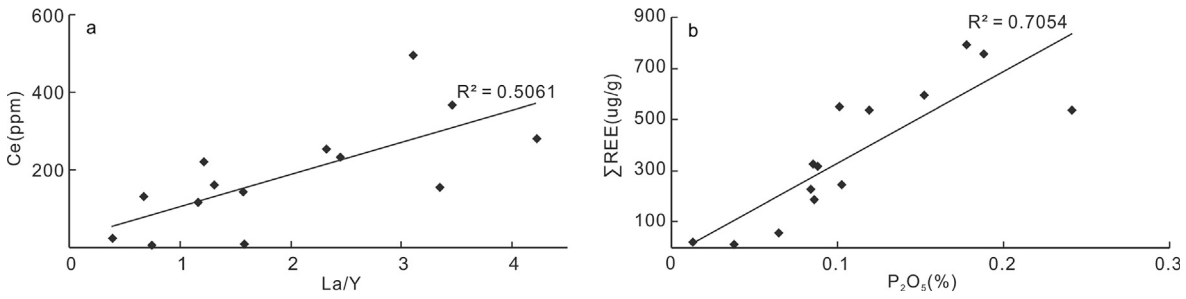

Fig. 11. Correlation analysis between Ce and La/Y ratios (a) and total REEs and P_2O_5 (b).

Fig. 12. Mass changes for major, trace, and rare earth elements with Ti as the immobile element during the weathering process from the felsic volcanics to the Poci bauxites: (a) the underlying clays; (b) bauxite ores.

clustering with Fe_2O_3 (Vind et al., 2018).

The assemblage of REEs-P_2O_5 reveals a potentially high affinity of REEs for phosphate, and even small amounts of phosphate may largely influence the REE signatures (Ma et al., 2002; Picard et al., 2002; Tyler, 2004). REEs can be released from primary minerals (phosphate, apatite, silicate and carbonate) as REE^{3+} ions into soil solution during weathering, which can be adsorbed by secondary phosphate minerals (as well as clay minerals, Fe and Mn-oxides, and carbonates) such as rhabdophane and crandallite group, which commonly occur during pedogenesis and bauxitization due to the dissolution of apatite in the parent rocks and have an important role in controlling REE contents and fractionations (Köhler et al., 2005; Stille et al., 2009; Berger et al., 2014; Sanematsu et al., 2015). The mobile REEs and phosphorus can also end up in oceans and be coupled as francolite and incorporated into sediments over time (Picard et al., 2002; Laveuf and Cornu, 2009; Emsbo et al., 2015).

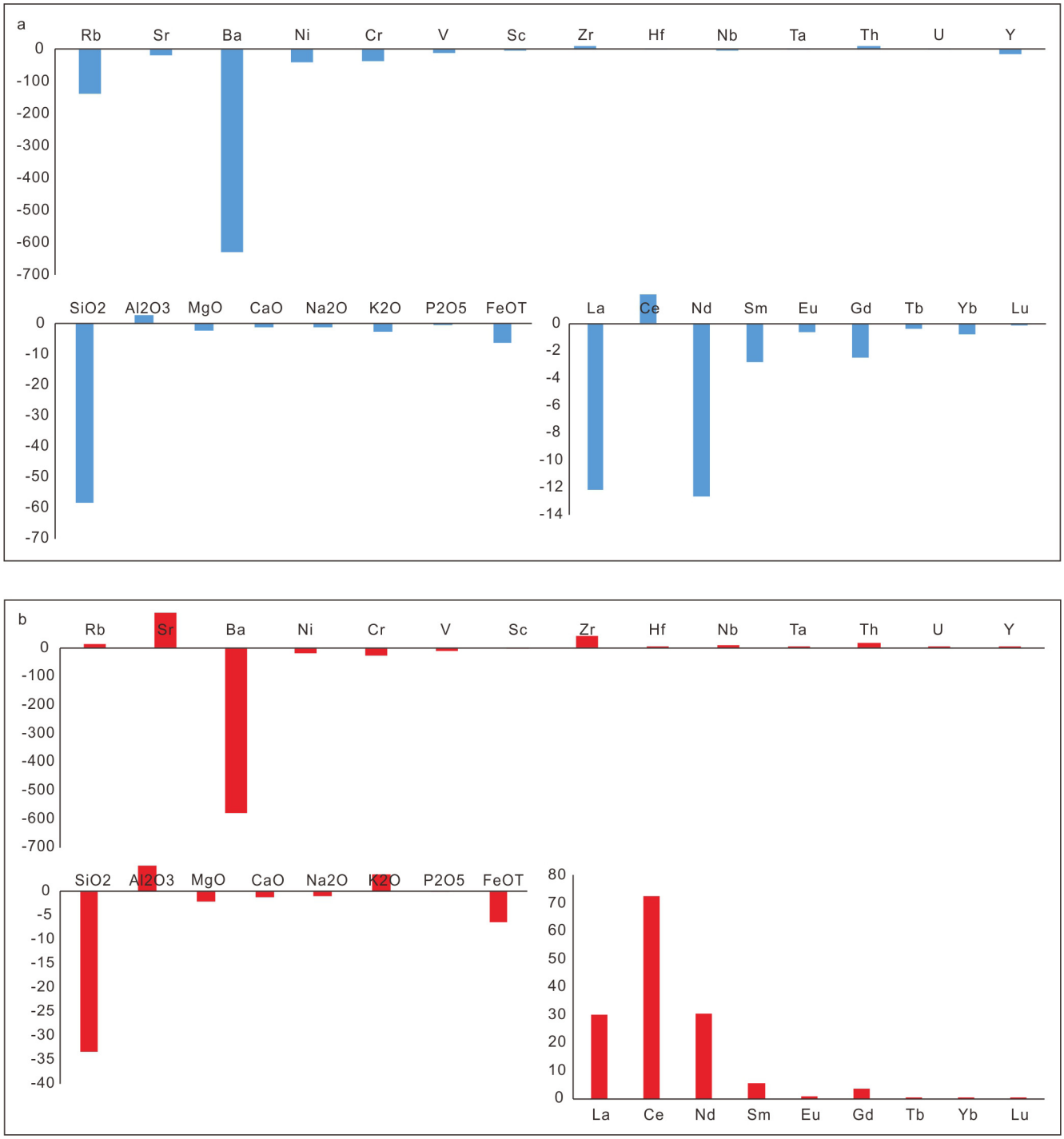

Fig. 13. Mass changes for major, trace, and rare earth elements with Ti as the immobile element during the weathering process from the PAAS to the Poci bauxites: (a) the underlying clays; (b) bauxite ores.

Elemental behaviors reflect the complicated results of inheritance from parent rocks, intense weathering, the change of redox and acid state, redeposition, burial and secondary alteration, diagenetic reworking, as well as epigenetic transformation (Bárdossy and Combes, 1999; Ahmadnejad et al., 2017). Therefore, the variation in elemental clustering revealed by Liu et al. (2013) and this study might be related to source rock heterogeneity, geochemical affinities of the given elements, and burial and secondary processes.

5.3. Mineral genesis during the bauxitization process

Mineral phases also reveal the protoliths and the ore-forming processes, such as transportation, chemical weathering, depositional environments, and post-depositional alteration. The Poci bauxite ores in western Henan mainly comprise diaspore and illite, which occur widely in the matrix, pisolites and concentric ooids. By contrast, the dominant clay minerals of the vast majority of karst bauxites of the world are kaolinite, with variable amounts of chlorite and minor amounts of illite minerals (Bárdossy and Combes, 1999; Zarasvandi et al., 2012; Yuste et al., 2017; Liu et al., 2016; Ahmadnejad et al., 2017 and references

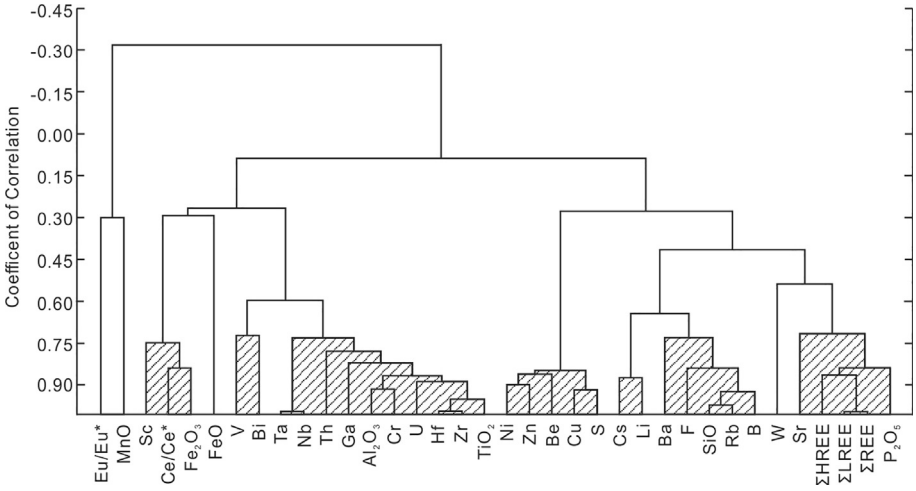

Fig. 14. Clustering analysis of major, trace and rare earth elements.

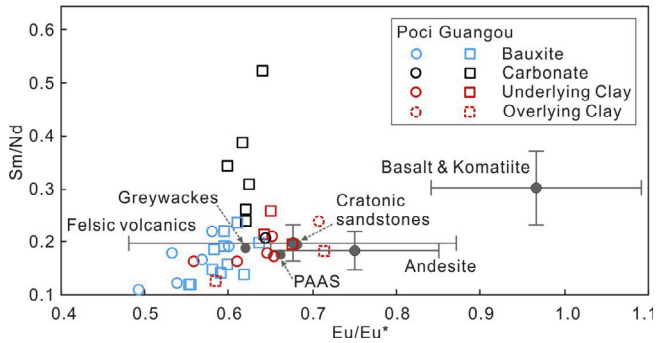

Fig. 15. Eu/Eu* vs Sm/Nd binary plot. PAAS data are from Taylor and Mclennan (1985); felsic volcanics, cratonic sandstones, andesite, basalt and greywackes data are from Condie (1993); Guangou data are from Liu et al. (2013).

herein).

Illite minerals in soils and weathered rocks are usually formed in three ways: 1) as secondary clays derived from the transformation of primary rock-forming minerals with similar properties (e.g. muscovite) (Meunier and Velde, 2004; Bétard et al., 2009), 2) as direct products of hydrothermal alteration after feldspar (Lonker and Fitz Gerald, 1990; Schleicher et al., 2006), or 3) as formation by meteoric processes in K-feldspar crystals due to partial dissolution (Pédro, 1997; Meunier and Velde, 2004; Bétard et al., 2009; Huggett et al., 2016). However, illite is also a common authigenic mineral in many siliciclastic sedimentary rocks (Ehrenberg and Nadeau, 1989; Huggett, 1995; Bjørlykke, 1998).

Although illite neoformation from K-feldspar ($KAlSi_3O_8$) could occur during the early stages of weathering in semi-arid environment (Bétard et al., 2009), illite is usually a transition phase during the bauxitization processes and will be transformed into kaolinite ($Al_2Si_2O_5(OH)_4$), which in turn, will be partially decomposed to form insoluble gibbsite ($Al(OH)_3$) and soluble hydrated silica as a result of weathering or early diagenetic processes during meteoric water flow at subsurface environment. More often, feldspars can be transformed into kaolinite and then gibbsite, and alternatively, be converted directly into gibbsite under humid tropical conditions (Gardner, 1972). Muscovite ($KAl_3Si_3O_{10}(OH)_2$) is a mica, which can be a primary mineral or secondary mineral transformed from K-feldspar. Illite minerals are chemically and structurally very similar to muscovite, but are typically deficient in alkalies, with less Al substitution for Si, and the general

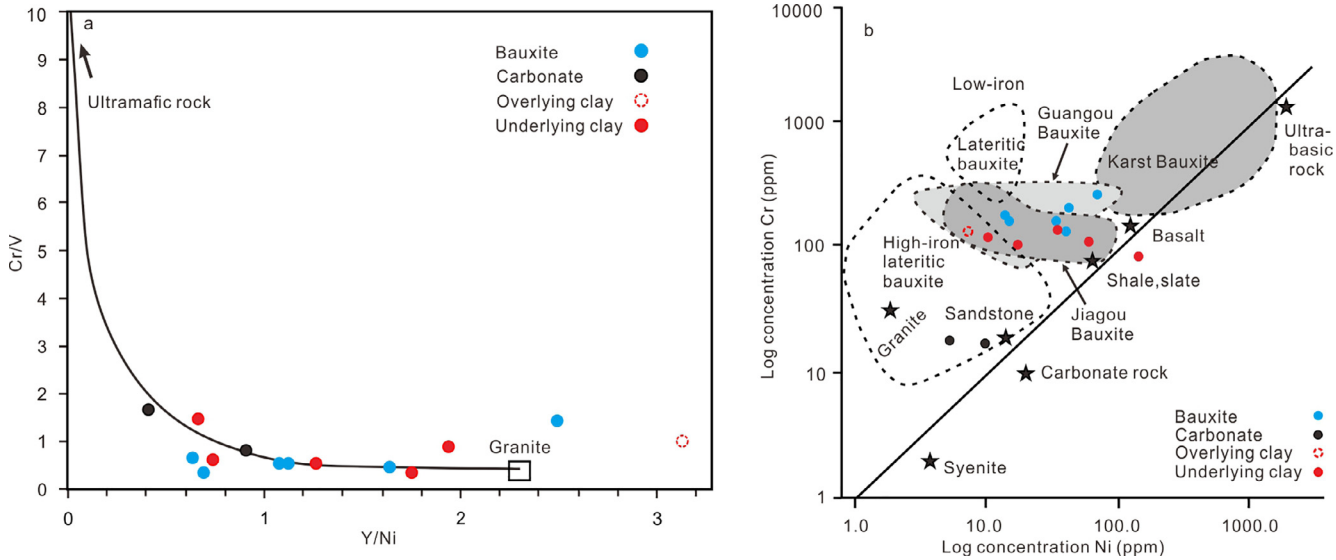

Fig. 16. Binary diagrams of Cr/V vs Y/Ni (a) and Cr vs Ni log contents (b) for potential precursor rocks (after Schroll and Sauer, 1968). All bauxites from western Henan, including the Poci bauxites, Guangou bauxites (Liu et al., 2013) and Jiagou bauxites (Wang et al., 2012) plot mainly between karst bauxite and high-iron lateritic bauxite.

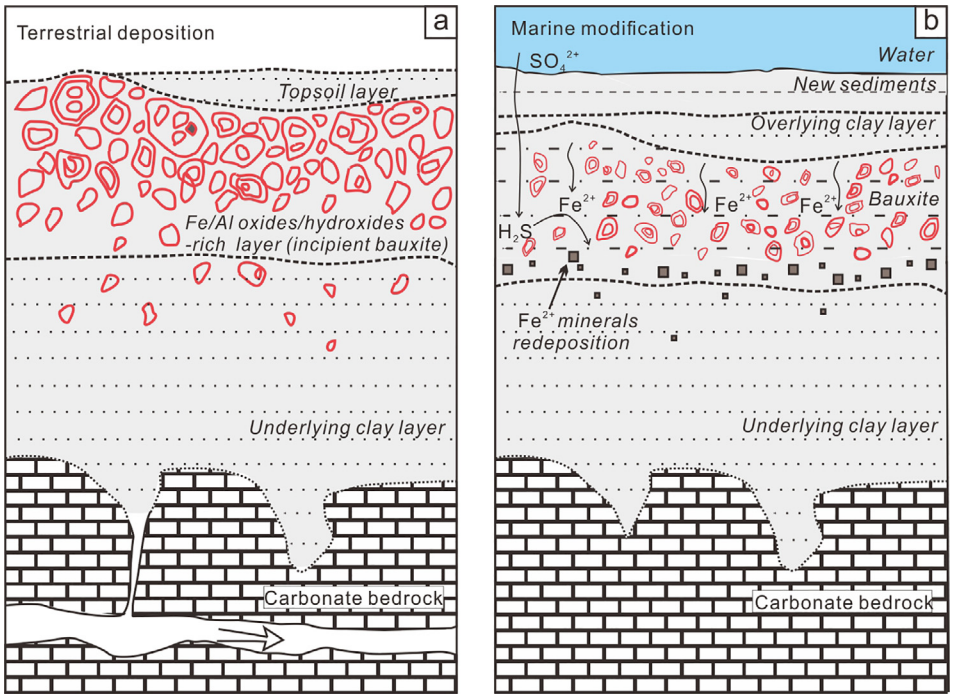

Fig. 17. Conceptual model for the formation and evolution of karst bauxites: a) terrestrial deposition of incipient bauxite materials with three layers (modified from Yang et al., 2018); b) marine modification showing Fe^{2+} is released from Fe oxides/hydroxides under the reducing conditions, migrates downward and re-precipitates at a lower depth (see text for more details).

formula for illite minerals can be written as $K_{0.88}Al_2(Si_{3.12}Al_{0.88})O_{10}(OH)_2$ (Rosenberg, 2002). Thus, these chemical reactions are shown as followings:

$$3KAlSi_3O_{8(Kspar)} + 2H^+ + 12H_2O \Leftrightarrow KAl_3Si_3O_{10}(OH)_{2(musco)} + 4H_4SiO_{4(aq)} + 2K^+ \quad (1)$$

$$2KAl_3Si_3O_{10}(OH)_{2(musco)} + 2H^+ + 3H_2O \Leftrightarrow 3Al_2Si_2O_5(OH)_{3(kaol)} + 2K^+ \quad (2)$$

$$KAl_3Si_3O_{10}(OH)_{2(musco)} + H^+ + 9H_2O \Leftrightarrow 3Al(OH)_{3(gibb)} + K^+ + 3H_4SiO_{4(aq)} \quad (3)$$

$$2KAl_3Si_3O_{8(Kspar)} + 2H^+ + 9H_2O \Leftrightarrow Al_2Si_2O_5(OH)_{4(kaol)} + 4H_4SiO_{4(aq)} + 2K^+ \quad (4)$$

$$Al_2Si_2O_5(OH)_{4(kaol)} + 5H_2O \Leftrightarrow 2Al(OH)_{3(gibb)} + 2H_4SiO_{4(aq)} \quad (5)$$

As such, during these chemical weathering processes, Si is released to solution as dissolved silica or silicic acid, written as aqueous H_4SiO_4. However, kaolinite and gibbsite become unstable at greater burial depth and higher temperatures, and gibbsite is usually transformed into boehmite and diaspore (Bárdossy, 1982; Denigres Filho et al., 2016), while the kaolinite tends to be reversed to illite (Ehrenberg et al., 1993; Beaufort et al., 1998; Bjørlykke, 1998; Lanson et al., 2002). According to the stratigraphic framework and depositional sequences in western Henan (Wang et al., 2012), the maximum burial depth of Poci bauxites is estimated to have reached below 3 km, allowing significant illitization to have occurred as a result of diagenesis (Ehrenberg and Nadeau, 1989; Bjørlykke, 1998). Compared to Poci bauxites, more kaolinite and less illite are present in the Guangou bauxites where plagioclase instead of K-feldspar is detected in the underlying clayey layer (Liu et al., 2013). Significant amounts of K-feldspar (microcline) was detected at the base of the underlying clayey layer (Table 1), indicating the supply of potassium in Poci bauxites is favorable for the formation of illite (Bjørlykke, 1998). The occurrence of kaolinite surrounded by illite revealed by Liu et al. (2013) gracefully suggests that illite clays are partially transformed from kaolinite when buried at great depth, rather than the direct weathering products or detrital minerals.

Goethite can be produced by chemical weathering from primary iron-bearing minerals or by the excretion processes by nitrate-reducing Fe^{2+}-oxidizing bacteria in a subaerial environment (Cornell and Schwertmann, 1996; Straub et al., 2004; Larese-Casanova et al., 2010). However, goethite is more usually considered to be pseudomorphs after siderite ($FeCO_3$), pyrite (FeS_2), and other Fe^{2+}-bearing minerals, which can be transformed into goethite when brought to the oxidizing zone (Bárdossy, 1982; Merinero et al., 2008; Liu et al., 2013). Pyrite, with variable amounts of siderite, often occur in karst bauxite profiles and were probably derived from alteration of Fe oxides/hydroxides that accumulated with the bauxites (Öztürk et al., 2002; Ellahi et al., 2017; Putzolu et al., 2018).

Based on the regional stratigraphy, ore deposit geology and mineralogy, especially iron mineral phases, we propose a formation model for the Poci bauxites, which is applicable to most of the world's karst bauxites (Fig. 17). The coal-bearing overlying sediments in the regional stratigraphic column (Yu et al., 2018) indicate reducing conditions during marine transgression, attributed to bacteria activities that oxidize organic matters and reduce sulfate (SO_4^{2-}) to hydrogen sulfide (Fig. 17b). All bauxites from western Henan and most of the world's karst bauxites are characteristic of the three-layer deposit structure, corresponding to the Quaternary terrestrial deposition of gibbsite nodules found in the carbonate platform of Yongjiang Basin (Yang et al., 2018), indicating that karst bauxites were mainly derived from terrestrial deposition of iron-rich bauxite materials. Mongelli and Acquafredda (1999) also proposed that the Fe-Al ooids in karst bauxites are usually formed in a pedogenic environment. Nevertheless, a subsequent modification in a submerged environment is to the benefit of further enrichment of aluminum. Fe^{2+} ions would be released from the Fe/Al oxides/hydroxides, combined with hydrogen sulfide and/or carbonate, and reprecipitated at a lower depth under the reducing conditions, generating an iron-rich bauxite horizon (Ellahi et al., 2017). This is well supported not only by the cubic shape of goethite found in the underlying clays (sample PC-2-4) which obviously are pseudomorphs after euhedral pyrite (Fig. 6b), but also by the goethite veins penetrating the ores indicative of the flow of Fe^{2+}-bearing solutions (Fig. 6d). Lammers et al. (2011) revealed that Fe oxyhydroxides can be partially transformed into sulfide phases and siderite when exposed to aqueous sulfide in contact with supercritical CO_2 at ~70–100 °C, and the relative yield of siderite to sulfide phases depends on the initial

sulfide concentration. However, Al is less soluble than Fe at low Eh and high pH conditions of marine sediments (Robb, 2005), and consequently, this marine modification would produce the high-grade bauxite horizon.

6. Conclusion

Poci bauxites are characterized by the association of diaspore-illite-anatase and high boron contents (176–1061 ppm). Geochemical investigations indicate boron is mainly hosted in illite, which are likely authigenic minerals transformed from kaolinite during diagenesis rather than unaltered detrital minerals. Mass change calculations reveal that Hf, Zr, Nb, Ta, U, Th, Sc, Cr, and Ga are stable relative to TiO_2 during the bauxitization process, indicating these elements are mainly associated with the anatase and diaspore. The bauxite horizons and the underlying clays are more enriched in ΣREEs and display more intense LREE/HREE fractionation than the overlying clays.

A conceptual model is proposed for the formation and evolution of karst bauxites. Collisions with adjoining arcs or terrains caused the uplift along the margins of NCC, and led to the formation of karstic topography, allowing felsic-dominated igneous rocks and siliciclastic materials to be transported to the low karst plain, and transformed into Fe/Al oxides/hydroxides-rich incipient bauxites under hot and humid tropical conditions. When the platform was submerged, Fe^{2+} ions were released from the iron-rich incipient bauxites under the reducing conditions, and reprecipitated at a lower depth, generating a high-grade bauxite horizon and an iron-rich bauxite horizon.

Acknowledgements

This research is jointly supported by the National Natural Science Foundation of China (No. 41672089), the National Basic Research Program of China (No. 2015CB452600), and the Fundamental Research Funds for the Central Universities of China (No. 2652015056).

References

Ahmadnejad, F., Zamanian, H., Taghipour, B., Zarasvandi, A., Buccione, R., 2017. Mineralogical and geochemical evolution of the Bidgol bauxite deposit, Zagros Mountain Belt, Iran: Implications for ore genesis, rare earth elements fractionation and parental affinity. Ore Geol. Rev. 86, 755–783.
Aubert, D., Stille, P., Probst, A., 2001. REE fractionation during granite weathering and removal by waters and suspended loads: Sr and Nd isotopic evidence. Geochim. Cosmochim. Acta 65, 387–406.
Babechuk, M.G., Widdowsonc, M., Kamber, B.S., 2014. Quantifying chemical weathering intensity and trace element release from two contrasting basalt profiles, Deccan Traps, India. Chem. Geol. 363, 56–75.
Bárdossy, G., 1982. Karst bauxites: Bauxite Deposits on Carbonate Rocks. In: Dev. Econ. Geol. Elsevier, Amsterdam, pp. 441.
Bárdossy, G., Aleva, G.J.J., 1990. Lateritic Bauxites: Developments in Economic Geology. Elsevier, Amsterdam, pp. 624.
Bárdossy, G., Combes, P.J., 1999. Karst bauxites: interfingering of deposition and palaeoweathering. In: Thiry, M., Simon-Coincon, R. (Eds.), Paleoweathering, paleosurfaces and Related Continental Deposits. International Association of Sedimentologists Spec. Publ. Blackwell science, pp. 189–206.
Bauer, A., Velde, B.D., 2014. Geochemistry at the Earth's Surface. Springer, Germany, pp. 136–145.
Beaufort, D., Cassagnabère, A., Petit, S., Lanson, B., Berger, G., Lacharpagne, J.-C., Johansen, H., 1998. Kaolinite-to-dickite conversion series in sandstone reservoirs. Clay Mineral. 33, 297–316.
Berger, A., Janots, E., Gnos, E., Frei, R., Bernier, F., 2014. Rare earth element mineralogy and geochemistry in a laterite profile from Madagascar. Appl. Geochem. 41, 218–228.
Bétard, F., Caner, L., Gunnell, Y., Bourgeon, G., 2009. Illite neoformation in plagioclase during weathering: evidence from semi-arid Northeast Brazil. Geoderma 152, 53–62.
Bjørlykke, K., 1998. Clay mineral diagenesis in sedimentary basins—a key to the prediction of rock properties. Examples from the North Sea Basin. Clay Miner. 33, 15–34.
Braun, J.J., Pagel, M., Muller, J.P., Bilong, P., Michard, A., Guillet, B., 1990. Cerium-anomalies in lateritic profiles. Geochim. Cosmochim. Acta 54, 781–795.
Braun, J.J., Pagel, M., Herbillon, A., Rosin, C., 1993. Mobilization and redistribution of REEs and thorium in a syenitic lateritic profile: a mass balance study. Geochim. Cosmochim. Acta 57, 4419–4434.
Calagari, A.A., Abedini, A., 2007. Geochemical investigations on Permo-Triassic bauxite horizon at Kanisheeteh, east of Bukan, West-Azarbaidjan, Iran. J. Geochem. Explor. 94, 1–18.
Condie, K.C., 1993. Chemical composition and evolution of the upper continental crust: contrasting results from surface samples and shales. Chem. Geol. 104, 1–37.
Cornell, R.M., Schwertmann, U., 1996. The Iron Oxides–structure, Properties, Reactions, Occurrence and Uses. VCH, Weinheim.
Couch, E.L., 1971. Calculation of paleosalinities from boron and clay mineral data. AAPG Bull. 55, 1829–1837.
Denigres Filho, R.W.N., Rocha, G.D.A., Montes, C.R., Vieira-Coelho, A.C., 2016. Synthesis and characterization of boehmites obtained from gibbsite in presence of different environments. Mater. Res. 19, 659–668.
Ehrenberg, S.N., Nadeau, P.H., 1989. Formation of diagenetic illite in sandstones of the Garn Formation Haltenbanken Area, Mid-Norwegian Continetnal Shelf. Clay Miner. 24, 233–253.
Ehrenberg, S.N., Aagaard, P., Wilson, M.J., Fraser, A.R., Duthie, D.M.L., 1993. Depth-dependent transformation of kaolinite to dickite in sandstones of the Norwegian continental shelf. Clay Mineral. 28, 325–352.
Ellahi, S.S., Taghipour, B., Zarasvandi, A., Bird, M.I., Somarin, A.K., 2016. Mineralogy, geochemistry and stable isotope studies of the Dopolan Bauxite Deposit, Zagros Mountain, Iran. Minerals 6, 11.
Ellahi, S.S., Taghipour, B., Nejadhadad, M., 2017. The Role of organic matter in the formation of high-grade Al deposits of the Dopolan karst type bauxite, Iran: mineralogy, geochemistry, and sulfur isotope data. Minerals 7, 97. https://doi.org/10.3390/min7060097.
Emsbo, P., McLaughlin, P.I., Breit, G.N., du Bray, E.A., Koenig, A.E., 2015. Rare earth elements in sedimentary phosphate deposits: solution to the global REE crisis? Gondwana Res. 27, 776–785.
Gamaletsos, P.N., Godelitsas, A., Kasama, T., Church, N.S., Douvalis, A.P., Göttlicher, J., Steininger, R., Boubnov, A., Pontikes, Y., Tzamos, E., Bakas, T., Filippidis, A., 2017. Nano-mineralogy and -geochemistry of high-grade diasporic karst-type bauxite from Parnassos-Ghiona mines, Greece. Ore Geol. Rev. 84, 228–244.
Gardner, L.R., 1972. Conditions for direct formation of gibbsite from K-feldspar–further discussion. Am. Miner. 57, 294–300.
Goldberg, S., Forster, H.S., Heick, E.L., 1993. Boron Adsorption Mechanism on Oxides, Clay Minerals, and Soils Inferred from Ionic Strength Effects. Soil Sci. Soc. Am. J. 57, 704–708.
Hanilçi, N., 2013. Geological and geochemical evolution of the Bolkardaği bauxite deposits, Karaman, Turkey: transformation from shale to bauxite. J. Geochem. Explor. 133, 118–137.
Harder, H., 1970. Boron content of sediments as a tool in facies analysis. Sed. Geol. 4, 153–175.
Huggett, J.M., 1995. Formation of authigenic illite in Paleocene mudrocks from the Central North Sea: a study by high resolution electron microscopy. Clays Clay Miner. 43, 682–692.
Huggett, J., Cuadros, J., Gale, A.S., Wray, D., Adetunji, J., 2016. Low temperature, authigenic illite and carbonates in a mixed dolomite-clastic lagoonal and pedogenic setting, Spanish Central System. Spain. Appl. Clay Sci. 132–133, 296–312.
Kabata-Pendias, A., Pendias, H., 2001. Trace Elements in Soils and Plants, third ed. CRC Press, Boca Raton.
Keren, R., Mezuman, U., 1981. Boron adsorption by clay minerals using a phenomenological equation. Clays Clay Miner. 29, 198–204.
Köhler, S.J., Harouiya, N., Chaïrat, C., Oelkers, E.H., 2005. Experimental studies of REE fractionation during water–mineral interactions: REE release rates during apatite dissolution from pH 2.8 to 9.2. Chem. Geol. 222, 168–182.
Lammers, K., Murphy, R., Riendeau, A., Smirnov, A., Schoonen, M.A.A., Strongin, D.R., 2011. CO2 sequestration through mineral carbonation of iron oxyhydroxides. Environ. Sci. Technol. 45, 10422–10428.
Lanson, B., Beaufort, D., Berger, G., Bauer, A., Cassagnabère, A., Meunier, A., 2002. Authigenic kaolin and illitic minerals during burial diagenesis of sandstones: a review. Clay Mineral. 37, 1–22.
Larese-Casanova, P., Haderlein, S.B., Kappler, A., 2010. Biomineralization of lepidocrocite and goethite by nitrate-reducing Fe (II)-oxidizing bacteria: effect of pH, bicarbonate, phosphate, and humic acids. Geochim. Cosmochim. Acta 74, 3721–3734.
Laveuf, C., Cornu, S., 2009. A review on the potentiality of rare earth elements to trace pedogenetic processes. Geoderma 154, 1–12.
Lerman, A., 1966. Boron in clays and estimation of paleosalinities. Sedimentology 6, 267–286.
Liu, X., Wang, Q., Feng, Y., Li, Z., Cai, S., 2013. Genesis of the Guangou karstic bauxite deposit in western Henan, China. Ore Geol. Rev. 55, 162–175.
Liu, X., Wang, Q., Zhang, Q., Zhang, Y., Li, Y., 2016. Genesis of REE minerals in the karstic bauxite in western Guangxi, China, and its constraints on the deposit formation conditions. Ore Geol. Rev. 75, 100–115.
Lonker, S.W., Fitz Gerald, J.D., 1990. Formation of coexisting 1 M and 2 M polytypes in illite from an active hydrothermal system. Am. Mineral. 75, 1282–1289.
Ma, Y.-J., Huo, R.-K., Liu, C.-Q., 2002. Speciation and fractionation of rare earth elements in a lateritic profile from southern China: identification of the carriers of Ce anomalies. Proceedings of the Goldschmidt Conference, Davos, Switzerland.
Maksimovic, Z., Panto, G., 1991. Contribution to the geochemistry of the rare earth elements in the karst-bauxite deposits of Yugoslavia and Greece. Geoderma 51, 93–109.
Mameli, P., Mongelli, G., Oggiano, G., Dinelli, E., 2007. Geological, geochemical and mineralogical features of some bauxite deposits from Nurra (Western Sardinia, Italy): insights on conditions of formation and parental affinity. Int. J. Earth Sci. 96, 887–902.
Merinero, R., Lunar, R., Martínez-Frías, J., Somoza, L., Díaz-del-Río, V., 2008. Iron oxyhydroxide and sulphide mineralization in hydrocarbon seep-related carbonate submarine chimneys, Gulf of Cadiz (SW Iberian Peninsula). Mar. Pet. Geol. 25, 706–713.

Meunier, A., Velde, B., 2004. Illite: Origin. Evolution and Metamorphism Springer, New York.
Mongelli, G., 1997. Ce-anomalies in the textural components of Upper Cretaceous karst bauxites from the Apulian carbonate platform (southern Italy). Chem. Geol. 140, 69–79.
Mongelli, G., Acquafredda, P., 1999. Ferruginous concretions in a Late Cretaceous karst bauxite: composition and conditions of formation. Chem. Geol. 158, 315–320.
Mongelli, G., Critelli, S., Perri, F., Sonnino, M., Perrone, V., 2006. Sedimentary recycling, provenance and paleoweathering from chemistry and mineralogy of Mesozoic continental redbed mudrocks, Peloritani mountains, southern Italy. Geochem. J. 40, 197–209.
Mongelli, G., Boni, M., Oggiano, G., Mameli, P., Sinisi, R., Buccione, R., Mondillo, N., 2017. Critical metals distribution in Tethyan karst bauxite: the cretaceous Italian ores. Ore Geol. Rev. 86, 526–536.
Mordberg, L.E., Stanley, C.J., Germann, A., 2001. Mineralogy and geochemistry of trace elements in bauxites: the Devonian Schugorsk deposit, Russia. Mineral. Mag. 65, 81–101.
Nesbitt, H.W., 1979. Mobility and fractionation of rare elements during weathering of a granodiorite. Nature 279, 206–210.
Öztürk, H., Hein, J.R., Hanilçi, N., 2002. Genesis of the Doğankuzu and Mortaş bauxite deposits, Taurides, Turkey: separation of Al, Fe, and Mn and implications for passive margin metallogeny. Econ. Geol. 97, 1063–1077.
Pédro, G., 1997. Clay minerals in weathered rock materials and in soils. In: Paquet, H., Clauer, N. (Eds.), Soils and sediments. In: Mineralogy and Geochemistry. Springer-Verlag, Berlin, pp. 1–20.
Picard, S., Lecuyer, C., Barrat, J.-A., Garcia, J.-P., Dromart, G., Sheppard, S.M.F., 2002. Rare earth element contents of Jurassic fish and reptile teeth and their potential relation to seawater composition (Anglo-Paris Basin, France and England). Chem. Geol. 186, 1–16.
Putzolu, F., Piccolo Papa, A., Mondillo, N., Boni, M., Balassone, G., Mormone, A., 2018. Geochemical characterization of bauxite deposits from the Abruzzi mining district (Italy). Minerals 8, 298.
Robb, L., 2005. Introduction to Ore-forming Processes. Blackwell Publishing, USA, UK, Australia, pp. 222–226.
Rosenberg, P.E., 2002. The nature, formation, and stability of end-member illite: a hypothesis. Amer. Miner. 87, 103–107.
Sanematsu, K., Kon, Y., Imai, A., Watanabe, K., Watanabe, Y., 2013. Geochemical and mineralogical characteristics of ion- adsorption type REE mineralization in Phuket, Thailand. Miner. Deposita 48, 437–451.
Sanematsu, K., Kon, Y., Imai, A., 2015. Influence of phosphate on mobility and adsorption of REEs during weathering of granites in Thailand. J. Asian Earth Sci. 111, 14–30.
Schleicher, A.M., Warr, L.N., Kober, B., Laverret, E., Clauer, N., 2006. Episodic mineralization of hydrothermal illite in the Soultz-sous-Forêts granite (Upper Rhine Graben, France). Contrib. Miner. Petrol. 152, 349–364.
Schroll, E., Sauer, D., 1968. Beitrag zur Geochemie von Titan, Chrom, Nickel, Cobalt, Vanadium und Molyb din in bauxitischen Gesteinen und das Problem der stofflichen Herkunft des Aluminiums. Travaux du ICSOBA 5, 83–96.
Snyder, R.L., Bish, D.L., 1989. Quantitative analysis. In: Bish, D.L., Post, J.E. (Eds.), Modern Powder Diffraction. Mineralogical Society of America, Washington, pp. 101–144.
Stille, P., Pierret, M.C., Steinmann, M., Chabaux, F., Boutin, R., Aubert, D., Pourcelot, L., Morvan, G., 2009. Impact of atmospheric deposition, biogeochemical cycling and water–mineral interaction on REE fractionation in acidic surface soils and soil water (the Strengbach case). Chem. Geol. 264, 173–186.
Straub, K.L., Schönhuber, W.A., Buchholz-Cleven, B.E.E., Schink, B., 2004. Diversity of ferrous iron-oxidizing, nitrate-reducing bacteria and their involvement in oxygen-independent iron cycling. Geomicrobiol. J. 21, 371–378.
Taylor, S.R., McLennan, S.M., 1985. The Continental Crust: Its Composition and Evolution. Blackwell, Oxford.
Tyler, G., 2004. Rare earth elements in soil and plant systems–a review. Plant Soil 267, 191–206.
Vind, J., Malfliet, A., Bonomi, C., Paiste, P., Sajó, I.E., Blanpain, B., Tkaczyk, A.H., Vassiliadou, V., Panias, D., 2018. Modes of occurrences of scandium in Greek bauxite and bauxite residue. Miner. Eng. 123, 35–48.
Wang, Q., Liu, X., Yan, C., Cai, S., Li, Z., Wang, Y., Zhao, J., Li, G., 2012. Mineralogical and geochemical studies of boron-rich bauxite ore deposits in the Songqi region, SW Henan, China. Ore Geol. Rev. 48, 258–270.
Wang, Q., Deng, J., Liu, X., Zhao, R., Cai, S., 2016. Provenance of Late Carboniferous bauxite deposits in the North China Craton: new constraints on marginal arc construction and accretion processes. Gondwana Res. 38, 86–98.
Williams, L.B., Hervig, R.L., Holloway, J.R., Hutcheon, I., 2001. Boron isotope geochemistry during diagenesis. Part I. Experimental determination of fractionation during illitization of smectite. Geochim. Cosmochim. Acta 65, 1769–1782.
Yang, S., Wang, Q., Zhang, Q., Chen, J., Huang, Y., 2018. Terrestrial deposition processes of Quaternary gibbsite nodules in the Yongjiang Basin, southeastern margin of Tibet, and implication for the genesis of ancient karst bauxite. Sed. Geol. 373, 292–306.
Yu, W., Algeo, T.J., Yan, J., Yang, J., Du, Y., Huang, X., Weng, S., 2018. Climatic and hydrologic controls on upper Paleozoic bauxite deposits in South China. Earth-Sci. Rev. https://doi.org/10.1016/j.earscirev.2018.06.014.
Yusoff, Z.M., Ngwenya, B.T., Parsons, I., 2013. Mobility and fractionation of REEs during deep weathering of geochemically contrasting granites in a tropical setting, Malaysia. Chem. Geol. 349–350, 71–86.
Yuste, A., Bauluz, B., Mayayo, M.J., 2017. Origin and geochemical evolution from ferrallitized clays to karst bauxite: an example from the Lower Cretaceous of NE Spain. Ore Geol. Rev. 84, 67–79.
Zarasvandi, A., Carranza, E.J.M., Ellahi, S.S., 2012. Geological, geochemical, and mineralogical characteristics of the Mandan and Deh-now bauxite deposits, Zagros Fold Belt. Iran. Ore Geol. Rev. 48, 125–138.